ACS APPLIED MATERIALS & INTERFACES

Research Article

www.acsami.org

Direct in Situ TEM Observation of Modification of Oxidation by the Injected Vacancies for Ni–4Al Alloy Using a Microfabricated Nanopost

Chong-Min Wang,*[†] Daniel K. Schreiber,[‡] Matthew J. Olszta,[‡] Donald R. Baer,[†] and Stephen M. Bruemmer[‡]

[†]Environmental Molecular Sciences Laboratory and [‡]Energy and Environment Directorate, Pacific Northwest National Laboratory, Richland, Washington 99352, United States

Supporting Information

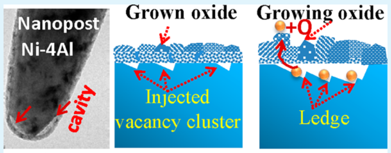

In-situ oxidation at 375 °C/0.5 mbar O_2

ABSTRACT: Vacancy injection and selective oxidation of one species in bimetallic alloy at high temperature is a well-known phenomenon. However, detailed understanding of the behavior of the injected vacancies and consequently their effect on oxidation remains elusive. The current research examines the oxidation of high-purity Ni doped with 4.1 at. % Al using in situ transmission electron microscopy (TEM). Experiments are performed on nanoposts fabricated from solution-annealed bulk material that are essentially single crystal samples. Initial oxidation is observed to occur by multisite oxide nucleation, formation of an oxide shell followed by cavity nucleation and growth at the metal/oxide interface. One of the most interesting in situ TEM observations is the formation of a cavity that leads to the faceting of the metal and subsequent oxidation occurring by an atomic ledge migration mechanism on the faceted metal surface. Further, it is directly observed that metal atoms diffuse through the oxide layer to combine with oxygen at the outer surface of the oxide. The present work indicates that injection of vacancies and formation of cavity will lead to a situation where the oxidation rate is essentially controlled by the low surface energy plane of the metal, rather than by the initial terminating plane at the metal surface exposed to the oxidizing environment.

KEYWORDS: *in situ TEM, oxidation, Ni–Al alloy, vacancy injection, cavity formation*

INTRODUCTION

Oxidation of metals and alloys has been well-studied and -documented in the literature.[1−4] Microscopically, an oxidation process can be generally described as the reaction of oxygen with the very surface layer of the metal to form a thin layer of oxide.[5] Upon the initial formation of an oxidation layer on the metal surface, the subsequent oxidation progresses by a combination of inward diffusion of oxygen and outward diffusion of metal ion through the oxide layer.[6−8] The rate of oxidation and consequently the microstructure of the oxidized product depend critically on the relative diffusivity of oxygen and metal ions through the oxide. If the diffusivity of metal ions through the oxide layer is faster than that of oxygen, the oxidation process will lead to the injection of vacancies into the system (commonly referred to as Kirkendall effect[9]). As a result, cavities may form by condensation of the vacancies.[10−18] As compared with a pure element, the oxidation behavior of a metallic alloy is further complicated by the presence of different cations, such as possibly involving selective oxidation of one component of the alloy.[15] Selective oxidation can be a disadvantage or an advantage for materials in oxidizing environments. For example, the oxidation and corrosion resistance of superalloys relies on the selective oxidation of Cr and Al to form protective surface layers of Cr_2O_3 and Al_2O_3, respectively, that significantly slow any oxidation of the underlying metal.[3,19] However, this same selective oxidation mechanism has also been linked to intergranular oxidation and susceptibility to stress corrosion cracking in high-temperature water environments in similar alloys when a protective film fails to form.[20] Oxidation of pure metals and its corresponding structural and chemical changes are determined by the dynamic interaction of diffusing species and defects, such as vacancies and grain boundaries. It has been generally realized that the oxidation rate is affected by the terminating crystallographic surface of the metal.[21] Despite these generalizations, it is not clear how the injection of vacancies and subsequent cavity formation affect the oxidation rate or process. It has been speculated that the formation of cavities may cut off the mass transport route and therefore slow the oxidation process.[10] However, the specific role of cavity has never been clearly visualized. On the other hand, formation of cavity upon oxidation will also directly affect the properties of the material. Formation of cavity will lead to a porous material or even peeling off the oxide shell, therefore leading to the weakening of the materials. This will directly affect the mechanical properties of the materials from the point of view of structural applications. It is of great importance to probe into details of the fine structural features of the oxide layer formed on metal surface upon oxidation.

Received: May 19, 2015
Accepted: July 17, 2015
Published: July 17, 2015

DOI: 10.1021/acsami.5b04341
ACS Appl. Mater. Interfaces 2015, 7, 17272−17277

In this work we report the direct in situ TEM observation of microstructural evolution of Ni doped with 4.1 at. % Al during oxidation. The oxidation experiment was carried out using aberration-corrected environmental TEM (ETEM), which allows establishing of up to 20 mbar pressure around the sample while in imaging mode. The sample is a nanopost that is machined out of a single-phase, bulk alloy in the solution-annealed and water-quenched condition. Due to the large grain size of the material, the microfabricated nanopost is essentially either a single crystal or a bicrystal at the tip of the nanopost. Therefore, the in situ TEM oxidation experiments provide us the opportunity for direct visualization of the dynamics microstructural and chemical evolution of a single crystal metallic material during high-temperature oxidation.[15,22,23] The present in situ TEM work gained unprecedented information regarding the role of cavity formation on the metal oxidation.

■ MATERIALS AND METHODS

The material studied in this work is high-purity Ni doped with 4.1 at. % of Al (thereafter designated as Ni−4Al). The alloy was hot-forged, then solution-annealed at 900 °C and water-quenched, resulting in a homogeneous single-phase alloy with a grain size of ∼100 μm. The bulk Al concentration was determined by inductively coupled mass spectroscopy to be 4.1 at. %, in good agreement with matrix measurements by atom probe tomography (APT).[24] Conventional focused ion beam (FIB) lift-out methods were used to extract and sculpt nanopost specimens of Ni−4Al in the same manner as ordinary specimens for APT with an apex diameter ∼ 100 nm.[25] Annular FIB milling was performed with 30 kV Ga^+ ions followed by 2 kV cleanup. Prior to in situ TEM experimentation, the nanoposts were field-evaporated by APT to remove residual Ga damage and implantation from the specimen surface. The ∼100 nm diameter and ∼3 μm long nanopost was nominally prepared as either a single crystal or bicrystal when selectively targeting inclusion of a grain boundary.

The in situ oxidation experiments utilized a dedicated field-emission ETEM (FEI Titan 80-300). The ETEM is equipped with an objective-lens spherical aberration corrector and controlled gas pressure around the sample using a differential pumping system. All of the oxidation experiments for in situ TEM were imaged at 300 kV. The specimen temperature was maintained at 375 °C using a resistant coil heating holder (Gatan, Pleasanton, CA, USA), and a pure O_2 atmosphere was set at 0.5 mbar around the sample. Note that, at these oxidizing conditions, both Ni and Al are expected to oxidize. The structural evolution of the nanoparticle during oxidation was continuously recorded at a rate of 2 frames/s.

Ex situ TEM was also performed with two probe aberration-corrected S/TEM microscopes (FEI Titan 80-300 operated at 300 kV and a JEOL JEM-ARM200CF operated at 200 kV). Selective area electron diffraction (SAED), high-resolution transmission electron microscopy (HRTEM), scanning TEM (STEM), high-angle annular dark field (HAADF) observations were conducted on an FEI Titan 80-300 microscope to probe the structure and chemical evolution at multiple scales. The STEM-HAADF images were collected by the annular detector in the range of 55−220 mrad. The electron beam has a convergence angle of 17.8 mrad. The elemental distribution in the nanopost before and after oxidation was mapped using energy dispersive X-ray spectroscopy (EDS). EDS was conducted on a JEOL JEM-ARM200CF microscope equipped with a JEOL SDD-detector with a 100 mm^2 X-ray sensor, enabling 10 times faster X-ray collections than traditional detector with excellent noise-to-signal ratio. The EDS quantification was performed using Analysis Station 3.8.0.52 (JEOL Engineering Co., Ltd.).

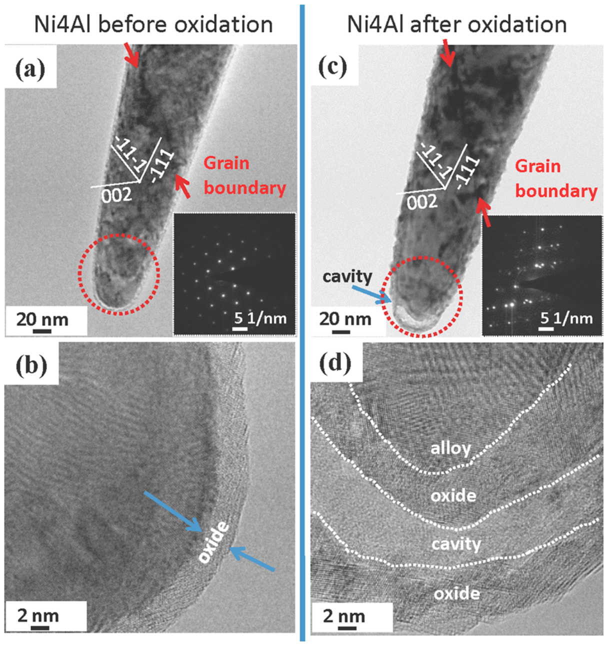

Figure 1. TEM images showing the microstructure of the FIB microfabricated nanopost of Ni−4Al sample for in situ TEM oxidation study. (a) The as-fabricated nanopost includes two grains with the grain boundary indicated by the red arrows. (b) HRTEM image of the as-fabricated post showing a crystalline oxide layer formed during the exposure of the sample in air (termed as initial oxidation). (c) Microstructure of the nanopost following oxidation at 375 °C in 0.5 mbar of O_2, revealing an oxide shell and cavity underneath the oxide layer. (d) HRTEM image of the oxidized nanopost, showing a crystalline oxide shell. The dashed circles in a and b indicate the regsion where the diffraction was taken.

■ RESULTS AND DISCUSSIONS

The structural feature of the as-fabricated Ni−4Al nanopost is shown in Figure 1a. Due to the large grain size of the bulk material, this nanopost contains two grains with the grain boundary across the middle of the nanopost. Therefore, the tip region of this nanopost is essentially a single crystal. Electron diffraction indicated that the tip region is oriented along the [110] zone axis. The bulk material has a nominal Al dopant concentration of 4% in atomic ratio. EDS quantitative analysis indicates that this nanopost contains 5.8% Al. The deviation of the EDS from the nominal doping level may be attributed to the errors related to background subjection and using a theoretical *k*-factor in the EDS quantification. The as-fabricated specimen was exposed to room temperature laboratory air after APT field evaporation, resulting in the formation of a thin layer of crystalline oxide as revealed by the HRTEM image shown in Figure 1b. Prior work[11,15,26] on nanoparticles has reported that the initial oxide formed on Ni has an epitaxial orientation relationship. However, this epitaxial orientation relationship is not maintained on the whole nanopost as demonstrated by the HRTEM images in Figure 1b. The nanopost shown in Figure 1a,b was further oxidized in the ETEM column at 375 °C with an O_2 pressure of 0.5 mbar, and the microstructural evolution was continuously monitored in situ during the oxidation. Figure 1c shows the general microstructure of the nanopost following in situ oxidation. The oxide layer has thickened significantly, and a cavity has formed at the tip region of the nanopost. The oxide layer formed during the high-temperature oxidation corresponds to a polycrystalline structure as illustrated in the HRTEM of Figure 1d. A dense outer oxide layer of ∼8 nm has formed at the very tip of the nanopost, under which a large cavity with ∼18 nm thickness has formed due to the condensation of the vacancies injected during the oxidation process. The polycrystalline nature

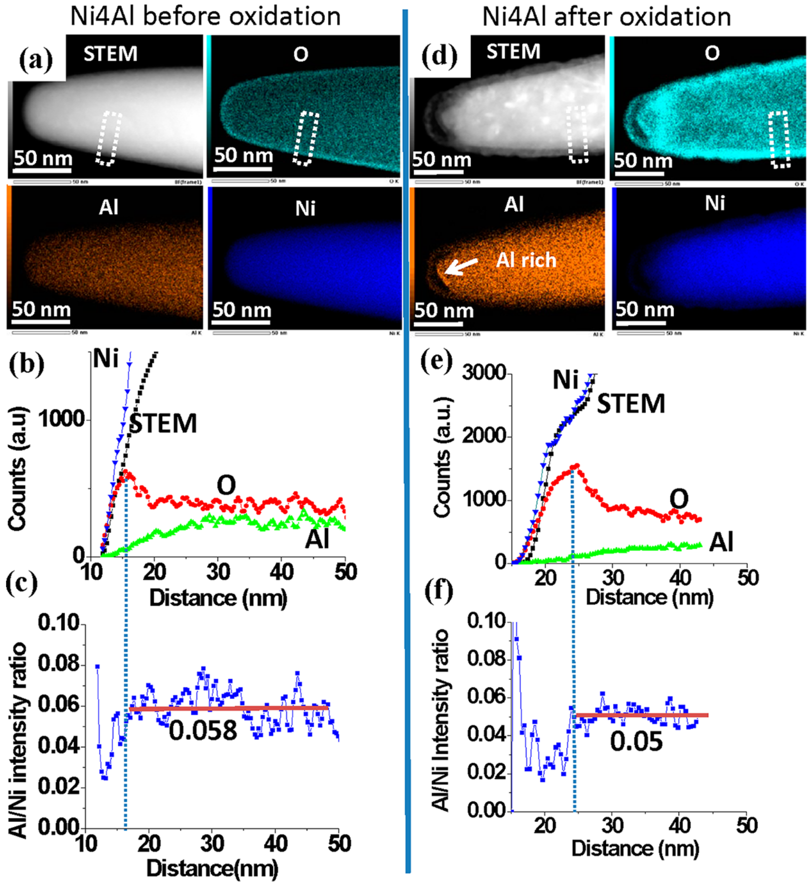

Figure 2. EDS mapping and Al/Ni atomic ratio in the oxide layer before and after the high-temperature oxidation. (a) STEM-HAADF image and elemental distribution maps of the as-fabricated nanopost. (b) The line scan intensity of the map along the dashed box indicated on the STEM image and the O map. (c) Al/Ni atomic ratio. Note the low concentration of Al in the oxide layer. (d) STEM-HAADF image and elemental distribution maps of the nanopost following the high-temperature oxidation. (e) Line scan intensity of the map along the dashed box indicated on the STEM image and the O map. (f) Al/Ni atomic ratio. Note the low concentration of Al in the oxide layer. The vertical dashed line marks the peak position of the oxygen map.

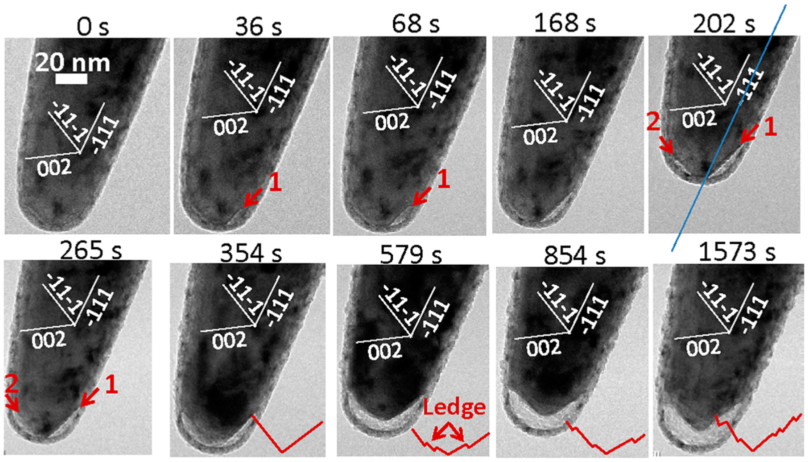

Figure 3. Captured video frame of time series TEM images showing the structural evolution of the Ni−4Al nanopost during oxidation at 375 °C in 0.5 mbar of O_2. Note the gradual thickening of the oxide layer and the formation of cavity due to condensation of injected vacancies. Two cavities indicated as 1 and 2 were nucleated at the interface between the oxide layer and the metal. Nucleation and growth of the cavity leads to the faceting of the metal under the oxide layer. The red line in the images after 354 s indicates the atomic ledges on the faceted metal surface.

of the oxide layer is also clearly revealed by the STEM-HAADF image shown in Figure 2d.

One of the key questions for the oxidation of metallic alloys is if the oxidation happens homogeneously for all of the components or one element is preferentially oxidized over the other. To explore if there was any selective oxidation for the case of Ni−4Al alloy, high-resolution EDS was used in a STEM to map the spatial distribution of Al, O, and Ni in the nanopost before and after high-temperature oxidation. Figure 2a displays the STEM-HAADF image and the corresponding elemental maps of the nanopost before oxidation. Figure 2b is the line scan intensity distribution of the white dashed line box in the O map, and the Al/Ni ratio is plotted in Figure 2c to indicate the Al distribution. The ratio of Al/Ni shows a valley within the oxide layer, suggesting a nonproportional oxidation of Al and Ni even during the initial oxidation. Similar EDS analyses were performed after the high-temperature oxidation with the elemental maps in Figure 2d, the line scan intensity in Figure 2e, and the ratio of Al/Ni across the oxide layer in Figure 2f. Similar to the initial oxidation results, the Al/Ni ratio in the oxide layer is lower than the bulk, indicating nonproportional oxidation of Al and Ni at high temperature. Another critical question that needs to be answered is the chemical composition of the oxide layer as it is Al_2O_3, NiO, or mixed. Based on the Al map in Figure 2d, it is apparent that the oxide shell is dominated by Ni and O, but also incorporating Al (see the very tip of the nanopost on the Al map). At the same time, as indicated in Figure 2d, there is a Al rich region near the tip of the oxidized nanopost (but within the cavity), indicating that accompanying the oxidation of Ni, Al is also oxidized and clustered together to form Al rich oxide. The true structural nature of the Al rich region is not determined. It most likely corresponds to alumina. Therefore, during the oxidation, Al shows a certain degree of selective oxidation. Overall, the observation of preferential oxidation of Al at dilute concentration is consistent with selective Cr oxidation in a Ni−Cr alloy.[1,3,27]

The microstructural evolution characteristics, especially the nucleation and growth of cavities, from Figure 1a,b to Figure 1c,d, during the oxidation are illustrated by the captured time series of TEM images shown in Figure 3 and in the Supporting Information (Movie S1). As oxidation progressed, two cavities nucleated at the metal/oxide interface. Cavity 1 is clearly visible at the 36 s image frame and then grows along the interface. A significant feature of the cavity growth is the faceting of the metal surface along a certain crystallographic plane. With continued oxidation and injection of vacancies, cavity 1 grows longer and wider with the same faceted metal surface. After slightly longer oxidation times (i.e., image frame of 202 s), cavity 2 is nucleated at the metal/oxide interface and also leads to the faceting of the metal surface. Due to the difficulty of judging if the faceted surface is edge on during the imaging, it is very hard to directly judge the faceting plane by a single image. A tomographic imaging and diffraction analysis is needed to determine the faceting plane. This is impossible for the current experimental setup of in situ oxidation work. Therefore, we only label the diffraction plane based on the diffraction pattern. With the continued oxidation and growth of both cavities 1 and 2, these two cavities coalesce as shown in the frame image of 354 s. Apparently, during the oxidation process, the atoms at the sharp apex were preferentially removed, leading to the morphological rounding of the apex as schematically drawn in the frame images of 579, 854, and 1573 s (the red line schematic drawings).

The growth of the cavity is the consequence of removal of metallic ions from the atomic ledge on the faceted metal surface and diffusion through the oxide layer to combine with oxygen. These features are illustrated by the captured time series frames shown in Figure 4. The images in row a of Figure 4 and the corresponding video in the Supporting Information (Movie S2) illustrate atomic ledge migration on the faceted plane that is approximately parallel with the electron beam direction. Similarly, the atomic ledge on the faceted plane that is approximately perpendicular with the electron beam also migrates as shown by the time series images presented in row b of Figure 4 and the video in Supporting Information (Movie S3). Atomic ledge migration has been recently observed on the very surface of the metal when it is exposed to oxidizing environment.[4] Removal of metallic atoms from the ledge and subsequently diffusion through the oxide layer not only account for the injection of vacancies and growth of the cavity but also most importantly it indicates that the formation of the oxide layer follows an oxide outward growth model. The outward growth of the oxide layer is clearly revealed by the captured HRTEM time series shown in Figure 5 and the corresponding video in the Supporting Information (Movie S4). As a typical example, the growth of an oxide bump is marked by the dashed red line and the red arrows indicate the growth direction. It can be seen that the oxide directly grows in the crystalline form and follows the atomic ledge growth mechanism.

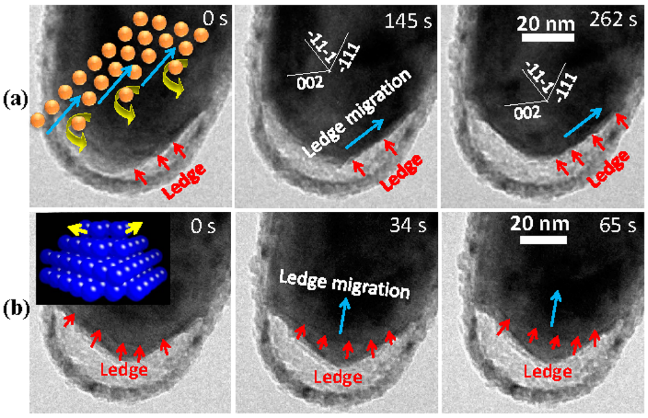

Figure 4. Captured video frames of time series TEM images of Ni−4Al oxidizing at 375 °C and 0.5 mbar of O_2 showing that, following the formation of cavity, the oxidation proceeds by atomic step peeling on the faceted plane, leading to the migration of atomic ledge. Row a shows the atomic ledge on the faceted plane and the peeling off atom leads the ledge migration as marked by the arrows. The insert in the 0 s image at row a shows a schematic model. Row b shows the atomic ledge on the plane that is projected on the paper plane. The insert in the 0 s image at row b is a schematic model.

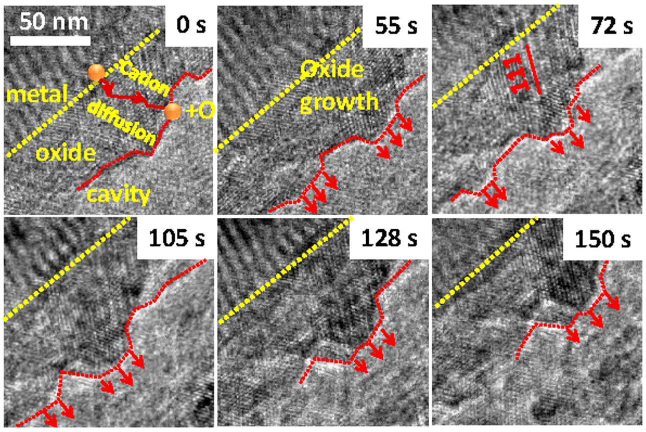

Figure 5. Captured video frames of time series HRTEM images of Ni−2Al oxidation at 375 °C and 0.5 mbar of O_2 directly revealing that the proceeding of oxidation follows the diffusion of metal ions through the oxide layer and combines with oxygen, leading to an oxide outward growth mechanism. The yellow dashed line marks approximately the boundary between the metal and the oxide. One of the growing oxides is marked by the red arrows.

Direct in situ TEM observation provides a clear picture of the oxide layer growth mechanism and how vacancy injection and clustering induce cavity formation at the metal/oxide interface. This process is schematically summarized in Figure 6, illustrating the initial oxidation and subsequent oxidation processes during high-temperature exposure. One of the most interesting in situ TEM observations is that cavity formation at the interface between the metal and the oxide layer can lead to the faceting of the metal surface. Following the faceting of the metal surface underneath the oxide layer, further oxidation entails the removal of metal atoms from the atomic ledge on the faceted metal plane. Due to the formation of the cavity, the surface diffusion will play a major role before the metal ion diffusion through the oxide layer to combine with oxygens.[11]

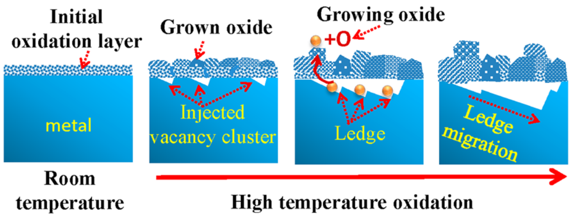

Figure 6. Schematic drawing showing the injection of vacancies leads to the nucleation of cavity at the interface between the metal and oxide layer. Formation of cavity leads to the faceting of the metal surface on the lower energy planes. Subsequent oxidation proceeds through the removal of metallic atoms from the ledge on the faceted plane, diffusing through the oxide layer and in combination with oxygen, yielding an outward growth of the newly formed oxide.

It has been generally believed that the oxidation rate of metal depends on the crystallographic orientation of the exposed metal surface.[21] The present observations that cavity formation leads to the faceting of metal surface indicates that the oxidation rate is essentially controlled by the low surface energy plane of the metal, rather than by the initial terminating plane of the metal that was initially exposed to the oxidizing environment. It should be pointed out that, due to the special geometry of the nanopost, the surface curvature affects the oxidation rate,[28] leading to the gradual thickness decrease when moving along the very tip of the nanopost toward the root of the nanopost. Therefore, the oxide layer formed at the apex of the nanopost is thicker than that at side of the nanopost. Furthermore, due to this curvature effect, the vacancies appear to preferentially condense at the tip region and therefore give the formation of the large cavity at the tip of the nanopost. However, this curvature effect will not affect the overall conclusion of the work.[11] It also should be noticed that if the oxide shell is not fully dense and the inside of the cavity is filled with oxidizing gas, consquently the metal surface within the cavity will be covered by an oxide layer. This is equivalent to the oxidizing of a fresh metal surface. If the cavity is not filled with the oxidizing gas, then the metal surface is free from oxide. For the current case, at the very beginning of the cavity formation, the surface of the metal is not covered with oxide, but late on, the surface is covered by oxide layer, leading to the oxide layer growth within the cavity as shown in Figure 4. For either case, the oxidation of metal proceeds as a ledge retreating as has been reported in our previous work.[15]

Although the cavity effect is manifested by the nanopost configuration, what is observed here vividly represents what happens during the metal oxidation. Therefore, the oxidation process proceeds in the following way. At the initial oxidation of the fresh metal surface, a dense oxide layer forms, which is accompanied by the injection of vacancies. Supersaturation of vacancies in both metal and the oxide layer will lead to the nucleation and growth of cavity at the interface between the metal and the oxide layer, leading to the exposure of a fresh metal surface. At the same time, the oxide shell will continuously evolve to a granular structure, which leads to the permeation of oxidizing gas into the cavity; consequently the metal surface was oxidized and covered by an oxide layer as happens during the initial oxidation. This process continues and leads to the oxide layer structure as shown in Figure 1.

■ CONCLUSION

The oxidation characteristics for a high-purity Ni−4Al alloy were investigated using in situ TEM imaging under dynamic oxidizing condition of 375 °C and 0.5 mbar of O_2. A single crystal nanopost sample was microfabricated out of a large-grain bulk alloy. The initial oxidation is featured by multisite oxide nucleation, followed by the formation of an oxide layer through growth and impingement of the oxides. Supersaturation of injected vacancies leads to the nucleation of cavities at the metal/oxide interface leading to the faceting of the metal under the oxide layer. Subsequent oxidation occurred by the removal of the metal atoms from the atomic ledge on the faceted plane and their diffusion through the oxide layer to combine with the oxygen, indicating an oxide outward growth mechanism. Cavity formation leading to the faceting of the metal surface indicates that the oxidation rate will be controlled by the faceted metal surface, rather than the initial metal surface exposed to the oxidizing environment.

■ ASSOCIATED CONTENT

Ⓢ Supporting Information

The Supporting Information is available free of charge on the ACS Publications website at DOI: 10.1021/acsami.5b04341.

Descriptions of movie files (PDF)
Movie S1 showing formation of cavity (AVI)
Movie S2 showing atomic ledge migration parallel with electron beam direction (AVI)
Movie S3 showing atomic ledge migration perpendicular to the electron beam (AVI)
Movie S4 showing oxide layer outward growth (AVI)

■ AUTHOR INFORMATION

Corresponding Author

*E-mail: Chongmin.wang@pnnl.gov.

Notes

The authors declare no competing financial interest.

■ ACKNOWLEDGMENTS

This work was supported by the U.S. Department of Energy (DOE), Office of Basic Energy Sciences. The work was conducted in the William R. Wiley Environmental Molecular Sciences Laboratory (EMSL), a DOE User Facility operated by Battelle for the DOE Office of Biological and Environmental Research. Pacific Northwest National Laboratory is operated for the DOE under Contract DE-AC06-76RLO 1830.

■ REFERENCES

(1) Yang, J. C.; Zhou, G. In Situ Ultra-High Vacuum Transmission Electron Microscopy Studies of the Transient Oxidation Stage of Cu and Cu Alloy Thin Films. *Micron* **2012**, *43*, 1195−1210.

(2) Zhou, G.; Slaughter, W. S.; Yang, J. C. Terraced Hollow Oxide Pyramids. *Phys. Rev. Lett.* **2005**, *94*, 246101.

(3) Hou, P. Y.; Stringer, J. The Effect of Aluminum as an Alloying Addition or as an Implant on the High-Temperature Oxidation of Ni-25cr. *Oxid. Met.* **1990**, *34*, 299−321.

(4) Qin, H. L.; Chen, X. D.; Li, L.; Sutter, P. W.; Zhou, G. W. Oxidation-Driven Surface Dynamics on NiAl(100). *Proc. Natl. Acad. Sci. U. S. A.* **2015**, *112*, E103−E109.

(5) Fromm, E. *Kinetics of Metal-Gas Interactions at Low Temperature: Hydriding, Oxidation, Poisoning*. Springer: Berlin, Heidelberg, New York, 1998.

(6) Railsback, J. G.; Johnston-Peck, A. C.; Wang, J. W.; Tracy, J. B. Size-Dependent Nanoscale Kirkendall Effect During the Oxidation of Nickel Nanoparticles. *ACS Nano* **2010**, *4*, 1913−1920.

(7) Cabrera, N.; Mott, N. F. Theory of the Oxidation of Metals. *Rep. Prog. Phys.* **1949**, *12*, 163−184.

(8) Chenna, S.; Banerjee, R.; Crozier, P. A. Atomic-Scale Observation of the Ni Activation Process for Partial Oxidation of Methane Using In Situ Environmental TEM. *ChemCatChem* **2011**, *3*, 1051−1059.

(9) Smigellkas, A. D.; Kirkendall, E. O. Zinc Diffusion in Alpha Brass. *Trans. AIME* **1947**, *171*, 130−134.

(10) Yin, Y.; Rioux, R. M.; Erdonmez, C. K.; Hughes, S. M.; Somorjari, G. A.; Alivisatos, A. P. Formation of Hollow Nanocrystals through the Nanoscale Kirkendall Effect. *Science* **2004**, *304*, 711−714.

(11) Wang, C. M.; Baer, D. R.; Thomas, L. E.; Amonette, J. E.; Antony, J.; Qiang, Y.; Duscher, G. Void Formation During Early Stages of Passivation: Initial Oxidation of Iron Nanoparticles at Room Temperature. *J. Appl. Phys.* **2005**, *98*, 094308.

(12) Fan, H. J.; Gosele, U.; Zacharias, M. Formation of Nanotubes and Hollow Nanoparticles Based on Kirkendall and Diffusion Processes: A Review. *Small* **2007**, *3*, 1660−1671.

(13) Nakamura, R.; Lee, J. G.; Mori, H.; Nakajima, H. Oxidation Behaviour of Ni Nanoparticles and Formation Process of Hollow NiO. *Philos. Mag.* **2008**, *88*, 257−264.

(14) Fan, H. J.; Knez, M.; Scholz, R.; Hesse, D.; Nielsch, K.; Zacharias, M.; Gosele, U. Influence of Surface Diffusion on the Formation of Hollow Nanostructures Induced by the Kirkendall Effect: the Basic Concept. *Nano Lett.* **2007**, *7*, 993−997.

(15) Wang, C. M.; Genc, A.; Cheng, H. K.; Pullan, L.; Baer, D. R.; Bruemmer, S. M. In-Situ TEM Visualization of Vacancy Injection and Chemical Partition During Oxidation of Ni-Cr Nanoparticles. *Sci. Rep.* **2014**, *4*, 3683.

(16) Wang, C. M.; Baer, D. R.; Amonette, J. E.; Engelhard, M. H.; Antony, J.; Qiang, Y. Morphology and Oxide Shell Structure of Iron Nanoparticles Grown by Sputter-Gas-Aggregation. *Nanotechnology* **2007**, *18*, 255603.

(17) Svoboda, J.; Fischer, F. D.; Vollath, D. Modeling of Formation of Binary-Phase Hollow Nanospheres from Metallic Solid Nanospheres. *Acta Mater.* **2009**, *57*, 1912−1919.

(18) Yin, Y.; Alivisatos, A. P. Colloidal Nanocrystal Synthesis and the Organic-Inorganic Interface. *Nature* **2005**, *437*, 664−670.

(19) Atkinson, H. V. A Review of the Role of Short-Circuit Diffusion in the Oxidation of Nickel, Chromium, and Nickel-Chromium Alloys. *Oxid. Met.* **1985**, *24*, 177−197.

(20) Gulsoy, G.; Was, G. S. Mechanism of Internal Oxidation of Alloy 617 in He-CO-CO2 Environments at 1123 K (850 C). *Metall. Mater. Trans. A* **2015**, *46*, 525−535.

(21) Boggs, W. E.; Kachik, R. H.; Pellissier, G. E. The Effects of Crystallographic Orientation and Oxygen Pressure on the Oxidation of Iron. *J. Electrochem. Soc.* **1967**, *114*, 32−39.

(22) Chenna, S.; Crozier, P. A. In Situ Environmental Transmission Electron Microscopy to Determine Transformation Pathways in Supported Ni Nanoparticles. *Micron* **2012**, *43*, 1188−1194.

(23) Jinschek, J. R. Atomic Scale Structure-Function Relationship of Heterogeneous Catalysts: Investigation of Gassolid Interactions by ETEM. *Microsc. Analy.* **2012**, *2012*, 5−10.

(24) Schreiber, D. K.; Olszta, M. J.; Bruemmer, S. M. Directly Correlated Transmission Electron Microscopy and Atom Probe Tomography of Grain Boundary Oxidation in a Ni−Al Binary Alloy Exposed to High-Temperature Water. *Scr. Mater.* **2013**, *69*, 509−512.

(25) Thompson, K.; Lawrence, D.; Larson, D. J.; Olson, J. D.; Kelly, T. F.; Gorman, B. In Situ Site-Specific Specimen Preparation for Atom Probe Tomography. *Ultramicroscopy* **2007**, *107*, 131−139.

(26) Wang, C. M.; Baer, D. R.; Bruemmer, S. M.; Engelhard, M. H.; Bowden, M. E.; Sundararajan, J. A.; Qiang, Y. Microstructure of the Native Oxide Layer on Ni and Cr-Doped Ni Nanoparticles. *J. Nanosci. Nanotechnol.* **2011**, *11*, 8488−8497.

(27) Atkinson, A. Transport Processes during the Growth of Oxide Films at Elevated Temperature. *Rev. Mod. Phys.* **1985**, *57*, 437−470.

(28) Stott, F. H. The Protective Action of Oxide Scales in Gaseous Environments at High Temperature. *Rep. Prog. Phys.* **1987**, *50*, 861−913.